Influence of geometric defects on the compression behaviour of thin shell lattices fabricated by micro laser powder bed fusion

Influence of geometric defects on the compression behaviour of thin shell lattices fabricated by micro laser powder bed fusion

Lei Zhang[a,d], Joseph Lifton[b], Zhiheng Hu[a], Ruochen Hong[c], Stefanie Feih[a,e*]

[a]*Singapore Institute of Manufacturing Technology (SIMTech), 73 Nanyang Drive, Singapore 637662*

[b]*Advanced Remanufacturing and Technology Centre (ARTC), 3 Cleantech Loop, #01-01, CleanTech Two, Singapore 637143*

[c]*Department of Mechanical Engineering, National University of Singapore, 9 Engineering Drive 1, Singapore 117575*

[d]*Department of Mechanical and Aerospace Engineering, Hong Kong University of Science and Technology, Kowloon, Hong Kong, China*

[e]*School of Engineering and Built Environment, Griffith University, Engineering Drive, Southport QLD 4222, Australia*

Published as:

Additive Manufacturing, 58, October 2022, 103038

* Corresponding author.

E-mail address: s.feih@griffith.edu.au (Stefanie Feih)

Abstract

Micro laser powder bed fusion (μLPBF) is an additive manufacturing process enabling the fabrication of thin-walled metallic shell lattices at the micrometre scale. With wall thicknesses reduced down to 100 μm, this process significantly enhances the structural design freedom, enabling the design of multi-functional, lightweight, stiff, and strong components. However, from a manufacturing perspective, as the wall thicknesses approach the printing resolution, this process is likely to introduce geometric defects, and informed quality assurance of the 3D-printed structures becomes critical. From a structural perspective, the mechanical properties of thin-walled structures are known to be highly sensitive to manufacturing defects. To quantify the process-induced geometric defects and to understand the influences of the geometric defects on the mechanical properties of thin shell lattices, we propose a micro X-ray computed tomography (XCT) based finite element (FE) modelling methodology, which is validated here for Primitive-type shell lattices fabricated by μLPBF in stainless steel. Four types of geometric defects, namely thickness variations, through-thickness defects (holes) on shell surfaces, surface waviness and roughness, are incorporated into the shell element-based FE models. The detailed evaluation of numerical and experimental compression tests results shows that the defect-informed simulation approach provides significantly improved prediction accuracy compared to the ideal geometry model in terms of stiffness, peak stress, plateau stress and densification behaviour. The respective influences of each type of defect and their combinations on the mechanical properties of the shell lattices are studied, highlighting that surface roughness and thickness variations lead to prominent impact on the reduction of both linear and nonlinear mechanical properties.

Graphical Abstract

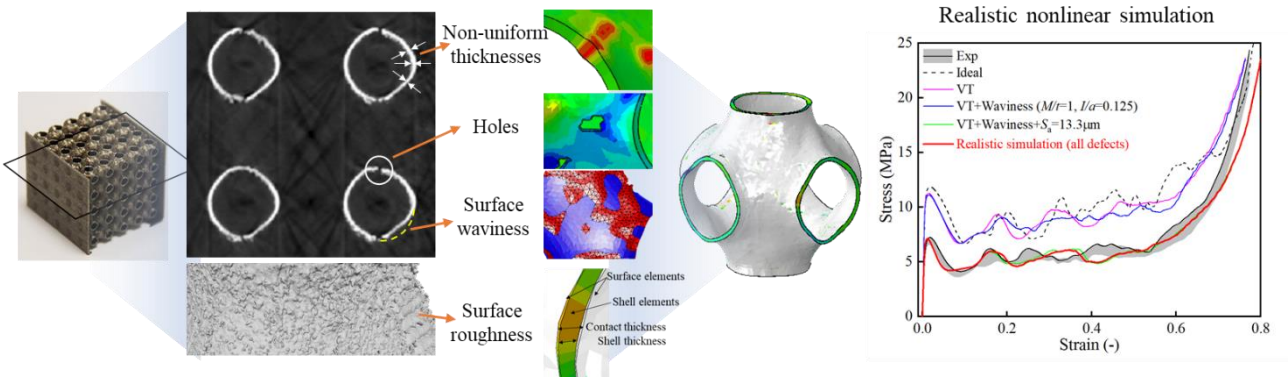

Key words: *Micro laser powder bed fusion; Thin shell lattices; X-ray computed tomography; Geometric defects; Finite element method*

1. Introduction

Shell lattice structures, composed of periodic non-intersecting and continuous thin shells, have received tremendous attentions due to their low densities, superior mechanical properties, and unique geometric characteristics among open-cell truss and shell-like lattices [1–5]. A wide range of applications based on metallic shell lattices have emerged, including lightweight components, energy absorbers, heat exchangers, electrodes, and bio-medical implants [6–8]. Micro laser powder bed fusion (μLPBF) is one of the promising techniques to fabricate metallic shell lattices with high resolution, low density, and low distortion [9]. Compared with the conventional LPBF technology, the main differences of μLPBF are the smaller laser spot size, finer powders, and smaller layer thickness, thus providing smaller minimum printable feature size (50 μm) and better surface finishing (R_a=1.3 μm) [9]. However, powder bed fusion processes introduce defects into the as-printed parts, resulting in deviations of their geometries and constitutive material properties away from the ideal designs and hence influencing the mechanical properties of lattices [6,10,11]. These defects and influences become increasingly prominent when the wall thickness approaches the printing resolution. Therefore, quantitative investigations on process-induced defects, their characterization and their influences are of great importance for lightweight shell lattices.

Two of the mostly studied LPBF-induced defects are (1) material and (2) geometric defects. The former includes undesired material inhomogeneities, anisotropy, voids, and cracks. The detection, characterization, formation mechanism and elimination methods of material defects have been comprehensively reviewed in [12–15]. An extensive number of studies have been devoted to controlling and eliminating internal cracks and voids through process optimization and post-process; however, it remains challenging to fully eliminate the AM process-induced material defects. For this reason, many studies have investigated the influence of material defects on the mechanical properties of LPBF fabricated lattices. For example, Amani et al. proposed a novel X-ray computed tomography (XCT) based finite element (FE) modelling method based on a double detector tomography technique (i.e., XCT with two different scales) to simulate the compressive behaviour of metallic truss lattices with heterogeneous internal voids [16]. It was found that the micro-voids decreased the Young's modulus slightly and more significantly the strength of AlSi10Mg lattices. The FE model allowed for a more accurate analysis of the stress-strain curves and fracture zones of lattices.

This work aims to study the latter issue of geometric defects, assessing types and distributions of defects and their respective influences on mechanical properties. Geometric defects of LPBF fabricated truss lattices, i.e., composed of slender struts, have been extensively investigated through scanning electron microscope (SEM) imaging and XCT. Major geometric defects are identified as strut thickness variations, non-circular cross-sections, strut waviness, missing struts and nodes, and surface roughness [17–22]. For example, Zanini et al. investigated the uncertainty determination methods of XCT measured dimensional accuracy for truss lattices using the substitution approach, achieving metrological traceability for measured strut diameters [23]. Rathore et al. developed an XCT method for dimensional measurement of lattices as well as their global distributions, and identified the elliptical cross-sections of as-printed lattices as compared with the nominal circular ones [24]. Liu et al. quantitively characterized strut oversizing, thickness variations, and waviness of LPBF printed lattices through XCT which was further used to develop simulation models of imperfect lattices [19]. Similarly, for shell lattices, geometric defects include thickness variations, through-thickness defects on shell surfaces (denoted as holes), surface waviness and surface roughness [3,4,21]. Although numerous efforts on process optimization and design compensation have been devoted to minimizing geometric defects for various types of lattices, remaining defects still exist due to the nature of the process and the complexity of lattice structures and need to be better understood and characterized [40]. Their presence can result in significant deviations of mechanical properties and a change to defect-triggered failure patterns compared to ideal designs. Related numerical and experimental studies have demonstrated that thickness variations, strut waviness, and irregular struct cross-sections can lead to significantly reduced stiffness [19,25,26], compressive strength [19,27], buckling strength [22], and fatigue resistance [26] for various types of truss lattices; while strut/node oversizing can result in increased tensile and bending stiffness of lattice structures [28,29].

Additive manufacturing (AM) process-induced geometric defects vary spatially and depend on the process, structure, and orientation, which complicates the accurate characterization of defects and numerical simulation of the mechanical properties for AM fabricated lattices. XCT technologies have offered powerful and non-destructive tools for addressing this challenge [14,30]. To this end, combined experimental and simulation efforts have been made to incorporate XCT data into FE models for lattices fabricated by AM. To date, there are two major types of FE models, based on either solid elements or structural elements such as beams and shells. Solid models typically include segmentation and mesh generation processes, and

result in a high-fidelity 3D geometric model for FE simulations [31]. Detailed features such as varying cross sections and irregular strut/node shapes can be captured. These models can predict the macroscopic and local mechanical behaviour of lattices more accurately. For example, Liverani et al. incorporated the XCT measured hole shapes (voids between struts) into FE models to improve the stiffness prediction accuracy of LPBF cobalt-chromium lattices [32]. Dallago et al. used XCT reconstructed models to investigate the stiffness, local stress distributions, and fatigue strength of LPBF lattices [26]. The XCT reconstructed FE model for polyurethane foams was shown to achieve good agreement with experimental results in terms of global stress-strain curves and local failure behaviour [31]. Melancon et al. proposed a XCT and statistical based FE modelling approach to predict the compressive stiffness and strength of Ti6Al4V lattices with reduced average errors (11% and 7.6%) compared with the as-designed models (49% and 41%) [33]. In addition, Cao et al. demonstrated that the XCT reconstructed solid models can predict the stress-strain curves for micro-stereolithography fabricated shell lattices with good accuracy [34]. However, the solid models are subject to heavy computational costs for mesh generation and FE computation due to the highly detailed volumetric mesh, since the minimum feature size is generally much smaller than the overall dimensions of a lattice sample. Therefore, this method was usually used for a sub-volume or a unit cell of a structure. In addition, the generation of solid models with controllable statistically distributed defects requires more advanced modelling and analysis techniques. For example, Korshunova et al. proposed an XCT-based binary random field method to efficiently generate statistical solid models based on XCT results and to further study the variability of lattice's Young's modulus using the finite cell method [35].

To reduce the computational costs while maintaining reasonable accuracy, FE models based on structural elements are favourable. For truss lattices, beam models with spatially varying cross-sectional properties can be generated based on the measurement of a series of struts from XCT images or reconstructed 3D models. Geometric defects including strut thickness variations, waviness, and missing struts can be captured by this method. The influences of these defects on the stiffness [26], compressive strength, global failure behaviour [19] and energy absorption performance [18] were investigated through the XCT based beam models including a large number of unit cells for various types of truss lattices. Furthermore, statistically distributed defects were generated and their influences on mechanical behaviour of lattices were studied via FE models based on beam elements, which provided insights on the statistical range of mechanical properties and deformations of imperfect lattices. The

combinations of statistic methods, such as Gaussian distribution [18,19,36] and Markov Chain [37], and high-fidelity simulations has enabled promising tools for predicting the mechanical properties and variability of AM fabricated lattices with stochastically distributed defects. However, while FE modelling methods incorporating AM-induced defects have been extensively developed for truss lattices, few studies exist for imperfect shell lattice structures in literature. So far, only shell element-based FE models for imperfect shell lattices with statistically distributed thicknesses were developed to study the effects of thickness variations on the mechanical properties [34]. The influences of other types of defects and their combinations on the mechanical properties of shell lattices remain unclear.

This paper introduces an XCT-based numerical methodology coupled with parametric studies enabling high-fidelity performance predictions, which in addition allows to quantitatively study the respective influences of various types of geometric defects on the Young's modulus, strength, and failure behaviour of μLPBF fabricated shell lattices. To this end, we propose an FE modelling method based on shell elements with variable thicknesses and offsets from the ideal position as measured from XCT results. Thin-walled Schwarz Primitive (P) surface shell lattices are fabricated by μLPBF with stainless steel 316L (SS316L), and then scanned through micro XCT and tested under compression loading. Four types of geometric defects are incorporated in shell models according to micro XCT characterization results: varying shell thicknesses, holes, surface waviness and roughness. Linear and nonlinear simulations are conducted to investigate the mechanical properties and the influences of these four types of defects on the compressive behaviour of P-shell lattices. Simulation and experimental results indicate that the proposed variable shell thickness models provide significantly improved prediction accuracy compared to the ideal models for the compressive modulus, plateau stresses and densification behaviour. Furthermore, sensitivities of mechanical properties with respect to each type of defects and their combinations are investigated by manipulation of the defect magnitudes in FE models. The parametric study reveals the effects of the defect type and magnitude on the performance reductions of shell lattices.

2. Experimental methods

2.1 Design of shell lattices

The Schwarz Primitive (P) surface, one of the well-studied triply periodic minimal surfaces (TPMS), is adopted here to create shell lattices. The P-surface can be described by nodal

approximations, and the corresponding shell lattices with constant thickness distributions are created by uniformly offsetting the mid-surface with a constant distance in both directions. The stereolithography (STL) files are generated by MATLAB scripting. In this work, each specimen for mechanical testing and for XCT-based dimensional measurements included 5×5×5 repeating unit cells with a cell size of 4 mm and two face plates with a thickness of 0.5 mm to minimize the boundary effect. In order to measure the surface roughness of as-printed specimens, additional smaller specimens with 2×2×2 unit cells were fabricated for high resolution XCT scanning.

2.2 Manufacture of thin-walled shell lattices using μLPBF

To fabricate thin-walled P-shell lattices in which the influences of defects are prominent, high resolution μLPBF with a small laser spot size, fine powders, and small layer thickness are favourable. In particular, the laser spot size, powder size, and layer thickness of conventional LPBF are usually in the range of 50-100 μm, 20-50 μm, and 20-100 μm, respectively; in contrast, these parameters for μLPBF are less than 40 μm, 25 μm, and 10 μm. As a result, μLPBF processes have been demonstrated to provide smaller minimum printable feature size (60 μm) and better surface finishing (R_a=1.3 μm) than conventional LPBF (minimum feature size of ~200 μm and R_a in range of 7-20 μm) [9], thus facilitating the realization of high resolution and lightweight structures.

Three lattice specimens were printed via an in-house developed μLPBF system, characterized and subsequently tested to determine the variation in mechanical performance [9]. Spherical stainless steel 316L powders ranging from 5 μm (D10) to 22.5 μm (D90) with an average diameter of 13.3 μm were used (supplied by AMC Powders Co., Ltd., Beijing). The in-house optimized process parameters (laser power: 60 W, laser spot size: around 15 μm, scanning speed: 600 mm/s, layer thickness: 10 μm) were adopted. The contour scanning strategy was used to approach the minimum printable thickness of thin-walled structures, in which two parallel scanning contours were generated by offsetting the P surface with a distance of 25 μm [38]. The adopted process parameters and scanning strategy resulted in wall thicknesses around 100 μm, lower than those achievable from conventional LPBF processes (150-200 μm). μLPBF processes were conducted under a N_2 atmosphere with an oxygen content of less than 200 ppm. After the μLPBF print, the dry weights of as-printed lattices were measured in dry air. The relative densities and volumes of lattice cores were calculated after

excluding the weights of face plates. The average shell thicknesses t were then calculated based on the formula $t=V/S$, where the V and S denote the volume of solid regions and the area of the ideal P-surface, respectively.

2.3 XCT scanning

X-ray computed tomography was used for dimensional measurements and defect characterization of as-printed P-shell lattices. In order to measure the dimensions and wall thicknesses of specimens, a Nikon XT H 225 ST X-ray system was used, with a voxel size of 23 um. The XCT scan settings are as follows: a source acceleration voltage of 210 kV, a source current of 80 µA, 2160 projections, and an X-ray filter of 0.5 mm of copper.

For the characterization of surface roughness, a high-resolution X-ray computed tomography scanning setup was applied to the smaller specimens as the length scale of surface roughness is much smaller than that of the shell thicknesses. Scanning with a high resolution generally reduces the scanning volume, so small specimens were used to achieve a sufficient spatial resolution. A Phoenix Vtomex M X-ray computed tomography system was used, with a voxel size of 4 µm. The XCT scan settings include a source acceleration voltage of 130 kV, a source current of 130 µA, 1000 projections with 3x averaging per projection, and an X-ray filter of 0.5 mm of copper.

2.4 Compression testing

Compression tests under displacement control were performed using an Instron 5982 universal test machine with a 10 kN load cell for three P-shell lattices. A strain rate of 1.0×10^{-3} /s (corresponding to a crosshead speed of 1.2 mm/min) perpendicular to the face plates was applied and each test stopped at 10 kN, leading to complete densification. Direct compressive displacements, δ, were measured via a linear variable differential transformer attached to compression plates to eliminate machine compliance. The deformation patterns of the shell lattices were recorded by a camera with a frequency of 0.5 Hz. The macroscopic stress, σ, and strain, ε, of shell lattices were calculated according to standard engineering assumptions with $\sigma=F/A_{\text{face}}$ and $\varepsilon=\delta/h$, where F, A_{face}, and h denote the compression force, face area, and height of specimen's core region, respectively.

3. FE models of imperfect shell lattices based on variable thickness shell elements

3.1 Characterization methods for geometric defects via XCT

XCT scanning results include a series of greyscale cross-sectional images and reconstructed 3D models of a specimen. Four types of geometric defects can be qualitatively identified for shell lattices as shown in Fig. 1: (a) shell thickness variations; (b) existing through-thickness holes in some thin-walled regions; (c) surface waviness, i.e., the mid-surface deviating from the ideal surface design; and (d) surface roughness in the form of metal powder particles.

To quantitatively characterize these defects and their spatial distributions for quality inspection and FE modelling purposes, we developed a shell thickness analysis method based on the measurement of 3D reconstructed geometries. The measured geometric defect distributions were further transferred to the shell element-based FE models as shown in Fig. 2. The process is described as follows. The 3D reconstructed models of the as-printed lattices were generated through segmentation on the image stack, which determined the structural boundary of solid materials and resulted in a triangulated surface model. The segmentation was performed using the thresholding method on the intensity values of the XCT images with a local surface correction tool within the commercial software Synopsys Simpleware 2019, resulting in the 3D reconstructed model shell lattices with non-uniform thicknesses. The thresholding value was selected to ensure the volume of XCT reconstructed model is equal to that from dry weight measurement which was used as the benchmark due to the traceability. With this 3D reconstructed model, a shell thickness analysis was performed based on a sphere fitting algorithm which defines the wall thickness as the largest local inscribed sphere fitted in the solid region. The shell thickness distributions were represented by point cloud data, whose locations were associated with the vertices of the reconstructed triangulated surface. It should be noted that the point cloud data do not directly represent the location and orientation of shell mid-surfaces. To link the as-printed shell thickness variations with the mid-surface of shells, the measured wall thickness data were converted to the ideal mid-surface of shell lattices by interpolation. In this work, the mid-surface of the ideal shell lattices was modelled by triangulated surfaces, and the shell thickness values at the mid-surface vertices were then calculated by an interpolation method performed on a set of scattered data, i.e., the point cloud data, using the MATLAB scatteredInterpolant function based on the algorithm in [39]. Prior to the interpolation, the point cloud data had to be aligned with the ideal geometries because they

are created in different coordinate systems. With the shell thickness distributions associated with the ideal mid-surface of shell lattices, it is then possible to establish the relation of thickness, location, and overhang angle of each triangular element for further statistical analysis and FE modelling. In this work, the segmentation of XCT images, shell thickness analysis, and data alignment were conducted using Simpleware, and the following interpolation and data analysis algorithms were developed in MATLAB 2019.

The thickness variations of μLPBF printed lattices are strongly orientation-dependent as reported in experimental measurements for truss lattices [17,40]. However, the thickness distributions have only been investigated for a few discrete overhang angles for truss lattices. In contrast, P-shell lattices include shell members with overhang angles continuously changing from 0º to 90º (0º represents shells parallel to the building direction), and therefore a systemic statistical analysis on the orientation dependency of shell thicknesses is obtainable.

The location and size of holes were not directly measured from the reconstructed models. Triangular elements with thicknesses below a minimum threshold, t_{min}, were considered as defects representing as through-thickness holes. The threshold can be adjusted to manipulate the hole size in the FE models.

The surface roughness was measured based on high resolution XCT data. In order to evaluate the surface roughness, regions of the sample's surface were extracted from the XCT data as a 3D point cloud. The surface form was removed by polynomial fitting, and thereafter the S_a roughness parameter was evaluated based on the method in [41]. Similar to shell thickness variations, the surface roughness is also strongly orientation dependent [21]; however, the roughness measurements for the complex curved surfaces at all locations are difficult. In this work, we measured the surface roughness at different locations with various overhang angles and an average surface roughness was adopted for simplicity. The measured surface roughness of upward (the projection of surface normal on the building direction is positive, see Figure 1 (b)) and downward surfaces is 5.5 ± 0.4 μm and 11.1 ± 0.3 μm, respectively.

The precise measurement of surface waviness for as-printed shell lattices is challenging because it is difficult to determine the mid-surface of the as-printed structures from the XCT data. In this work, a random waviness function with controlled magnitudes and "wavelength" was generated and applied to the ideal surface. First, random numbers following a uniform distribution were generated in regular girds with specified magnitudes and spatial intervals, representing the magnitude and "wavelength" of waviness, respectively. The random numbers

were considered as the surface deviation from the ideal surface to the imperfect ones. Second, the surface deviation at the vertices of the ideal mid-surface was computed by interpolation, and the vertices were moved along the normal direction to generate a waved surface.

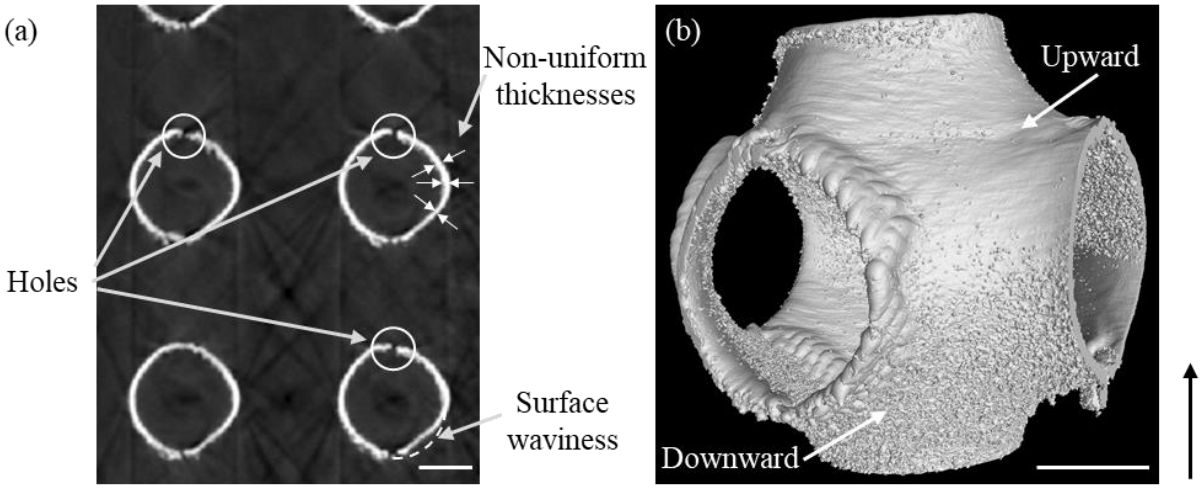

Fig. 1. Geometric defects of as-printed P-shell lattices identified through X-ray CT scanning. (a) Non-uniform thicknesses, holes, and surface waviness in a 2D slice with the scanning voxel size of 23 μm. (b) Surface roughness shown in a 3D reconstructed model with the scanning voxel size of 4 μm. The black arrow represents the building direction. Scale bar: 1 mm.

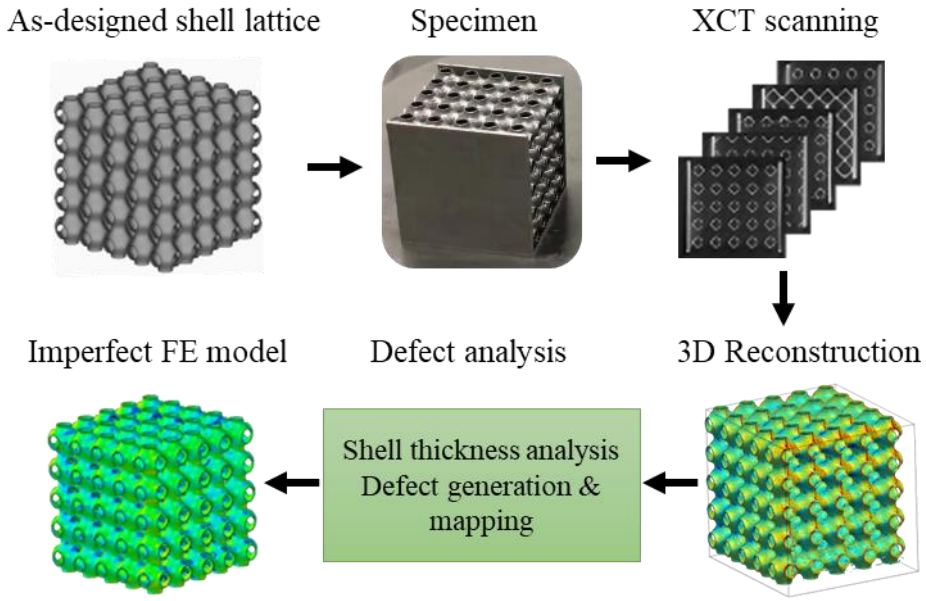

Fig. 2. The flowchart of defect analysis and generation of imperfect FE models based on variable thickness shell elements.

3.2 FE models of imperfect shell lattices with variable thickness shell elements

To incorporate the four types of geometric defects into FE simulations and to study their influences on the elastic, nonlinear properties, and failure behaviour of shell lattices, we develop an XCT-based FE modelling method coupled with parametric defect studies based on variable thickness shell elements. FE simulations are conducted with FE package Abaqus 2019. The FE models include 5×5×5 repeating unit cells and face plates, which is the same configuration as for the tested specimens. Since the shell thickness to unit cell size ratio is about 1/40, shell elements can achieve high accuracy in FE analysis. The mesh of shell lattices is directly adopted from the triangulated surface of the ideal or waved mid-surfaces, because they are associated with the geometric defects in defect analysis described in Section 3.1.

Linear triangular shell elements (S3 for Abaqus/Standard and S3R for Abaqus/Explicit) with an average edge length of around 0.15 mm are assigned to the mesh of shell lattices. The mesh of the shell lattice core includes about 190K nodes and 370K elements. A mesh refinement study shows that this mesh can achieve a balance of computational efficiency and analysis accuracy (see Appendix A). Two face plates meshed with linear hexahedral elements (C3D8R) are tied with the lattice cores. To incorporate shell thickness variations, the nodal thicknesses of shell elements obtained in Section 3.1 are directly imported into Abaqus through a discrete field input. Holes are modelled by deleting the elements whose thicknesses are smaller than the prescribed threshold. Surface waviness is generated by moving the nodes of shell elements representing the mid-surface along the normal direction.

Attached particles with limited interconnectivity (see Fig. 1(b)) are a major cause of surface roughness. Based on the assumption that these particles do not contribute to structural stiffness and strength, but contribute to contact behaviour, surface roughness is modelled by uniformly reducing the shell thickness while maintaining the contact thickness. The reduction of shell thickness will directly reduce the Young's modulus and strength of lattices. Modification of the contact thickness for shell elements is implemented by using additional layers of surface elements defined at both sides of the mid-surface with controllable offset distance. These additional surface elements have no mechanical stiffness and strength, are tied with the mid-surface, and follow the deformation of the mid-surface. The distances between two surface elements are based on the XCT measured thickness, and contact establishes once the surface elements touch each other regardless of the thickness reduction of shell elements. Therefore, the shell and contact thicknesses and their responses of shell models are decoupled. Simply reducing the shell thicknesses was found to delay the contact initiation according to the authors'

previous results [4]. The modification of contact thicknesses is shown to improve the prediction accuracy of densification behaviour, which is primarily contact dominated.

The base material stainless steel 316L is modelled with an isotropic material with a Young's modulus of 202 GPa, Poisson's ratio of 0.3, 0.2 % offset yield strength of 653 MPa and isotropic hardening behaviour characterized by standard tensile tests according to ASTM E8M with dog-bone shaped specimens [38]. Material defects such as anisotropy and internal voids are not considered in this work.

Linear FE simulations are conducted in the Abaqus/Standard solver. The four types of geometric defects are included in these models. Surface roughness in linear models is incorporated by reducing shell thickness, while the modification of contact thicknesses is not included as no contact is established in the elastic region. The bottom plate is fixed in all degrees of freedom, and a small displacement load in the *z*-direction is applied to the top plate. The compressive stress and strain are calculated from the displacement and reaction force, respectively. The Young's modulus of shell lattices along the *z*-direction is calculated. It is noted that material plasticity and geometric nonlinearity are not modelled in linear simulations.

Nonlinear FE simulations are conducted in the Abaqus/Explicit solver. Here, the plasticity of stainless steel 316L is included. Contacts of shells and face plates are modelled with hard normal behaviour and a friction coefficient of 0.2 for tangential behaviour. Surface elements are modelled in nonlinear simulations to mimic the contact behaviour of a shell lattice with high roughness, with a high density of 8×10^{7} g/cm^{3} to avoid deep penetrations during contact. To mimic the experimental setup, the bottom plate is fixed in all degree of freedoms, while the displacement is applied to a rigid compression plate which contacts with the top plate of the lattice. A smoothly loaded compressive strain up to 0.8 is applied to the rigid compression plate through displacement control.

4. Results and discussion

4.1 Shell thickness analysis

The whole spectrum of overhang angles (ranging from 0-90°) is evenly separated into 9 intervals with 10^{o} in each, and the probability density distributions of shell thicknesses for representative angle intervals are evaluated and shown in Fig. 3. The histogram (Fig. 3 (a)) shows a decreasing trend of average wall thicknesses with increasing overhang angles, with the lowest thickness observed for surfaces built parallel to the building platform. The standard

deviation of shell thicknesses also exhibits an orientation dependency, with the maximum existing at 40-60º overhang angles. The overall statistical average shell thickness and standard deviation of the as-printed P-shell lattices are 106.8 and 20.3 μm, respectively. The statistical average thickness agrees well with the average thickness (108.0 μm) evaluated from the measured relative density of the lattices (6.41 % ± 0.05 %). The probability density functions of shell thicknesses within three selected overhang angle intervals are shown in Fig. 3 (b-d). It is found that the probability density functions of thicknesses generally exhibit non-symmetric distribution characteristics.

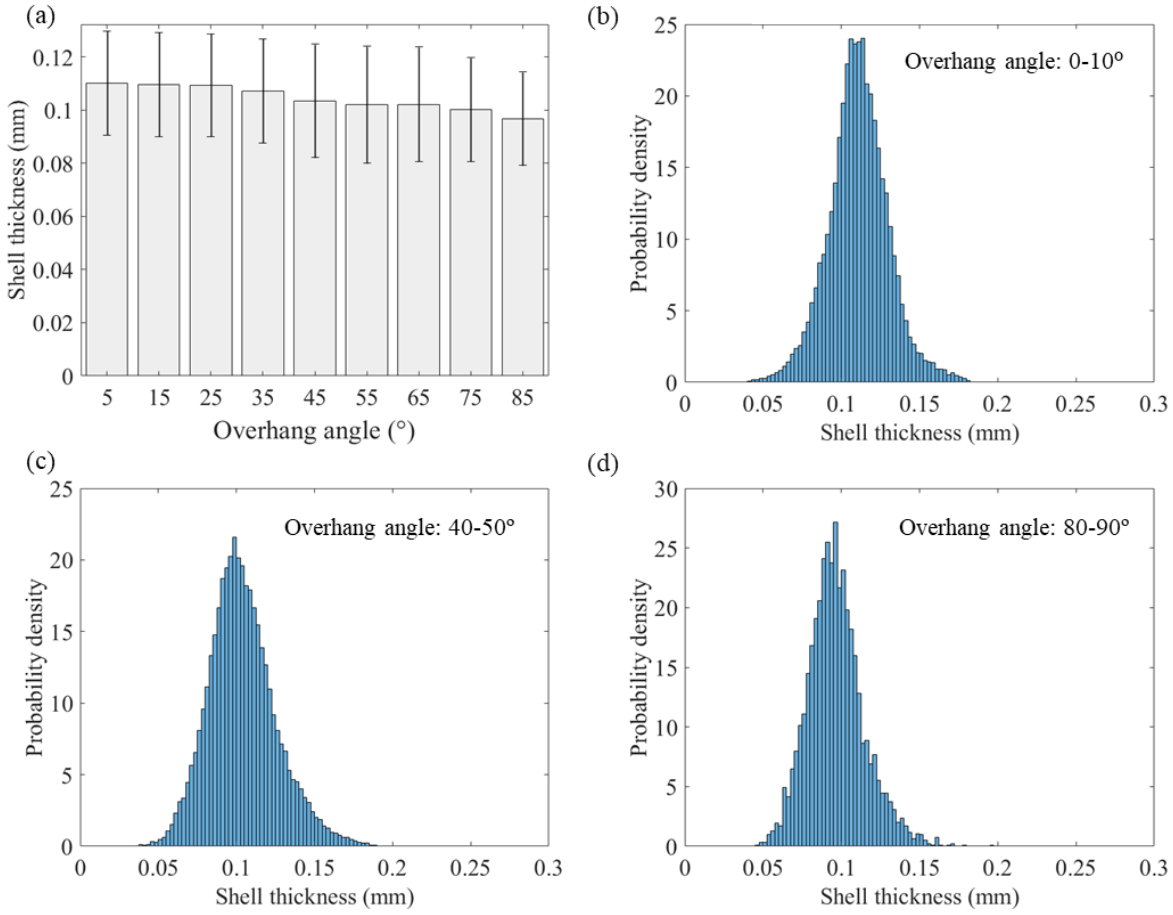

Fig. 3. Measured thickness distributions of P-shell lattices with respect to the overhang angle. (a) An overview of the area-weighted means and standard deviations of wall thicknesses for all overhang angle intervals. (b, c, d) Probability density distributions of thicknesses with overhang angles within 0-10º, 40-50º, and 80-90º, respectively.

4.2 Mapping of geometric defects in FE model geometry

A unit cell of the full lattice structure is cropped from the XCT reconstructed model as an example to illustrate the proposed variable shell thickness FE models. The unit cell with shaded representing thicknesses measured from 3D reconstructed model is shown in Fig. 4 (a). The FE model of the ideal mid-surface with mapped and rendered thickness variations and a threshold thickness of 65 μm for holes (Fig. 4 (b)) shows that the proposed FE mapping methodology reproduces the thickness distributions in a good agreement with the reconstructed model. The locations and values of thick and thin shells in the FE model are consistent with those in the XCT reconstructed model. Feature sizes about 100 μm or above can be well captured by the proposed method as the XCT scanning resolution is 23 μm. Smaller features, such high-frequency thickness variations, are filtered out according to the size of the shell elements. It should be noted that in Fig. 4 (a) left, the shell thicknesses are about 10 μm in dark blue regions, so holes are likely to exist at these locations. For these locations whose adjacent regions are thin shells, the holes are captured in the FE model; however, holes cannot be identified using the proposed thickness interpolation method if the adjacent regions are thick shells (see the circles in Fig. 4 (a) right).

Waved mid-surfaces of the P-shell lattice with a magnitude of 108.0 μm and spatial normalized intervals by the unit cell size I/a=0.125, 0.25, 0.5 are overlayed with the ideal mid-surface in Fig. 4 (c), where I and a denote the spatial interval and unit cell size. A small spatial interval represents high-frequency waviness. The corresponding FE models including waviness and thickness variations are shown in Fig. 4 (d).

The surface roughness of μLPBF printed parts mainly results from the attached particles as can be seen in Fig. 1 (b). As the attached particles do not contribute to the mechanical stiffness and strength as a solid material layer, surface roughness is modelled by reduced shell thicknesses (coloured elements) and surface elements (grey surfaces) as shown in Fig. 4 (e)). The distances between two surface elements are equal to the thicknesses in Fig. 4 (d) to maintain contact thickness.

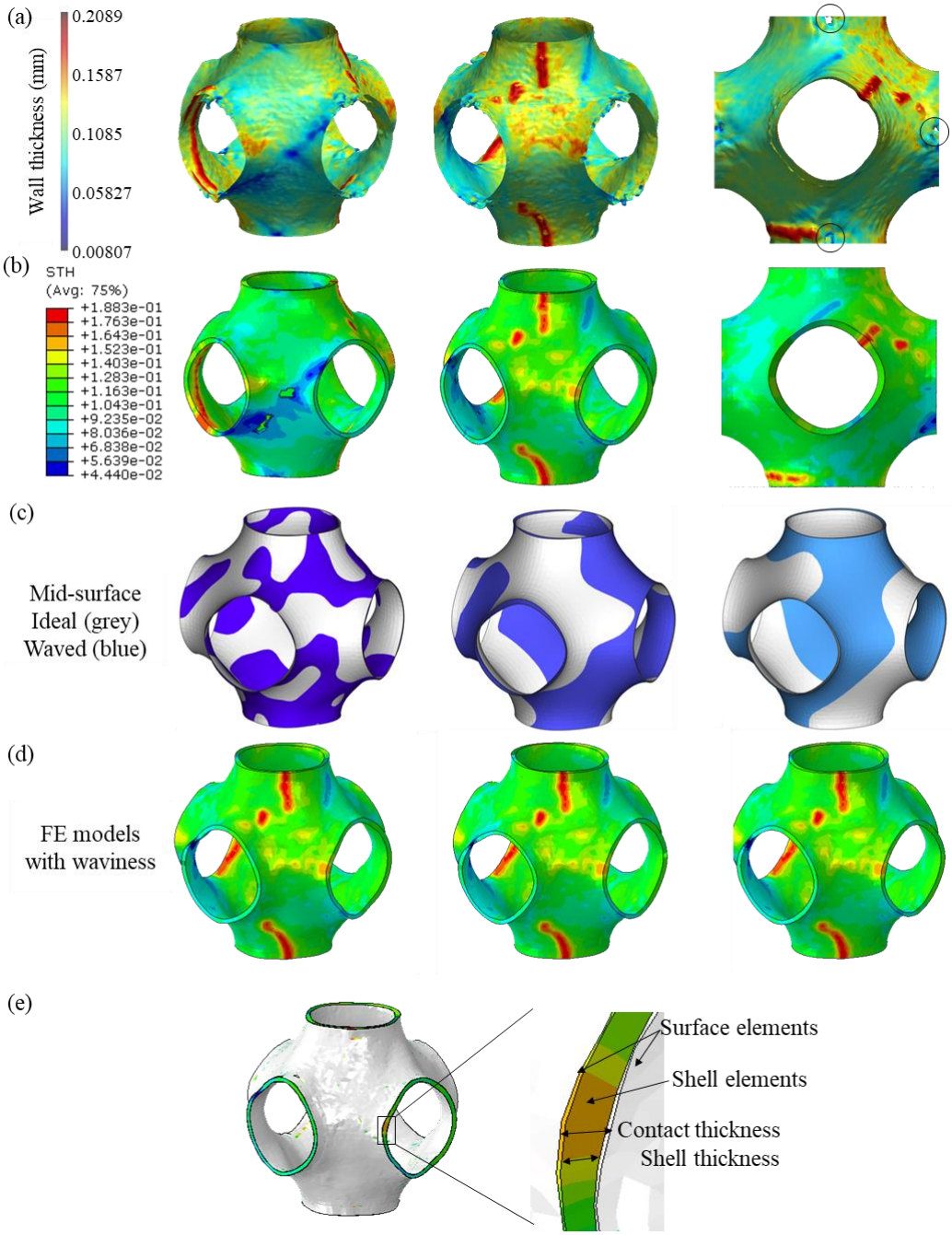

Fig. 4. Illustration of the proposed variable shell thickness FE model using a unit cell of P-shell lattices. (a) Wall thickness analysis results of the printed structure via its XCT-reconstructed model. (b) FE models with mapped variable shell thicknesses and holes. (c) Waved mid-surface (blue) of shells with normalized spatial interval *I/a* of 0.125, 0.25, 0.5 (from left to right, respectively) in comparison with the ideal mid-surface (grey). (d) FE models with surface waviness corresponding to (c), mapped variable shell thicknesses and holes. (e) FE model with mapped variable shell thicknesses, holes, waviness, and surface roughness. The rendering of shell thickness is enabled in (b, d, e) for visualisation purposes of thickness variations, and the colour plots represent shell thicknesses (STH) in mm.

To summarize, the proposed variable shell thickness FE model can easily capture the geometric thickness variations and surface roughness, which are directly measured from XCT results. Through-thickness hole defects are partially identified according to the small thickness regions. Surface waviness is generated from random magnitudes and an assumed "wavelength". The imperfect shell models are used for the study of the influences of AM-induced geometric defects on the mechanical properties of shell lattices. The proposed XCT-based shell modelling methodology is well suited for analysing thin shell lattices due to the relatively high computational efficiency and reasonable accuracy. In addition, the magnitude of defects can be readily adjusted to study the defect sensitivity in a parametric manner. Each type of defect can be activated/deactivated, which is a useful tool to study the interactions between different types of defects.

In the following defect sensitivity analysis, the influences of geometric defects and their magnitudes on the mechanical properties of lattices are studied through activating/deactivating defects and manipulating their magnitudes. The magnitude ranges considered in this work are listed in Table 1. The thickness variations characterized from shell thickness analysis are directly mapped in the FE model. The range of surface roughness is from 0 to 13.3 μm, with the upper bound of the average powder size. A roughness value S_a=0 μm represents the deactivated roughness defect. The selected upper bound of S_a is based on the average particle size of 13.3 μm as attached powder particles were considered to be the main contributors to surface roughness. The upper bound is greater than the measured maximum surface roughness because the measured S_a value is defined as the arithmetical mean height of a surface compared with the mean surface, which may underestimate the thickness of the attached particles. It is shown that considering a S_a value equal to the average powder size results in good agreement between FE and experimental results as detailed in section 4.6. The surface roughness normalized by the measured average shell thickness S_a/t ranges from 0 to 0.12. The hole area normalized by the total mid-surface area A_h/A_0 varies from 0 to 1.2 %, corresponding to a small amount of holes observed in XCT scanning. The ranges of the magnitudes and "wavelength" of waviness considered in this work are estimated based on visual inspection of XCT results (Fig. 1). We estimate that the "wavelength" of waviness is comparable to or smaller than the unit cell size, and the magnitude is comparable to wall thickness, hence the wave magnitude normalized by the average shell thickness M/t ranges from 0 to 2, and the normalized spatial interval I/a ranges from 0.125 to 0.5. Normalized spatial intervals lower than 0.125 are not studied because high-frequency waviness is not observed in XCT results.

Table 1. The magnitude ranges of geometric defects considered in defect sensitivity analysis.

Type of defects	Lower bound	Upper bound
Surface roughness S_a/t (-)	0	0.12
Hole area A_h/A_0 (%)	0	1.2
Wave magnitude M/t (-)	0	2
Spatial interval I/a (-)	0.125	0.5

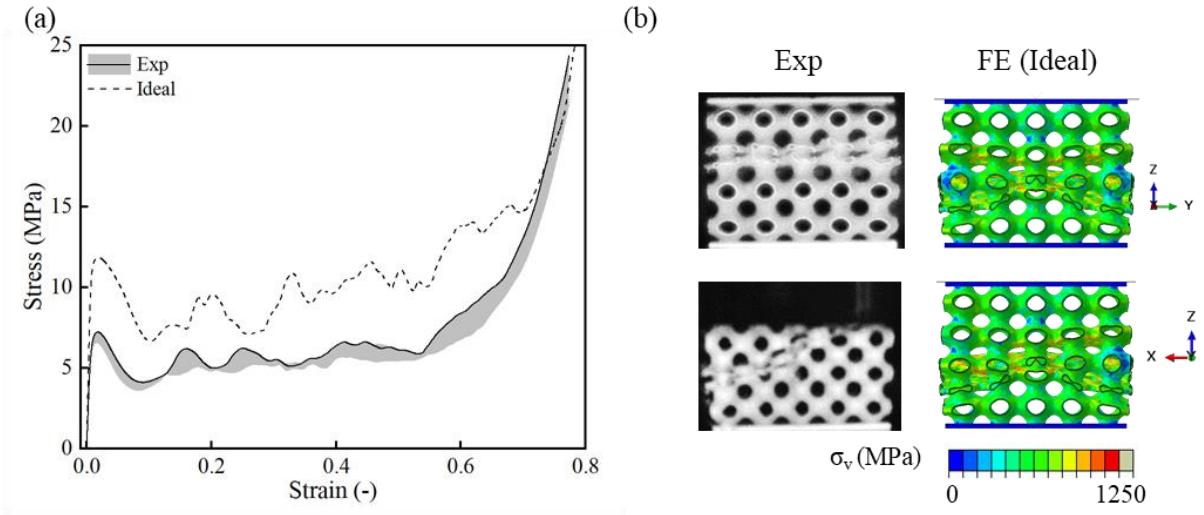

Fig. 5. (a) Stress-strain curves and (b) deformations at ε=0.24 of P-shell lattices from experimental results and the ideal FE model. FE deformations are shaded by contours of von Mises stress σ_v of shells. In the bottom figure of the experimental deformations, the field of view of one intact layer (top left) and two collapsed layers (top right) was reduced by the compression platen; however, the presented images adequately validate the single shear band deformation.

4.3 Compression test results

The density of stainless steel 316L measured by the Archimedes' method is 7.95 g/cm^3. The measured relative density of P-shell lattices is 6.41 % ± 0.05 %, and the corresponding average shell thickness is t=108.0 μm. The representative stress-stain curves of P-shell lattices with shaded experimental variation domain based on the three test results are shown in Fig. 5 (a). The curves display a typical compression behaviour of lattices including a linear region, stress plateau outlining the various local and global failure characteristics, and finally the densification regions occurring once neighbouring TPMS shell come into contact with each

other. The failure of the low-density P-shell lattices results in the development of a diagonal shear band mode for all specimens (see Fig. 5 (b)). The compressive properties along *z*-direction are summarized in Table 2 for the experimental data, the ideal FE model, and selected models with incorporated defects. Differences in properties and failure behaviours for structures with parametric defect variations are discussed in the following sections.

Table 2. Compressive properties of P-shell lattices from experimental and nonlinear simulation results. VT denotes variable thickness.

Model	Young's Modulus (GPa)	Peak stress (MPa)	Plateau stress (MPa)
Experiment	1.03 ± 0.02	6.80 ± 0.31	5.23 ± 0.28
Ideal	1.99	12.20	9.26
VT	1.91	11.25	8.25
VT + Waviness (M/t=1, I/a=0.125)	1.81	11.11	8.62
VT + Waviness (M/t=1, I/a=0.125) + S_a=13.3 μm	1.28	7.12	5.52
VT + Waviness (M/t=1, I/a=0.125) + S_a=13.3 μm + Hole 0.12 %	1.27	7.11	5.43

4.4 Numerical prediction characteristics with the ideal model

The ideal FE model is considered to have a uniform thickness of 108.0 μm (corresponding to the same volume to the measured results of as-printed lattice cores) and is used to benchmark the influences of geometric defects on the compressive performance of lattices. The Young's modulus of the ideal model, E_0, as calculated by the linear numerical model, is 1.99 GPa. The fully nonlinear stress-strain curve from the explicit FE model is shown in Fig. 5. The Young's modulus, the first peak stress and plateau stress of the ideal model are significantly higher (over 75 %) than those of experimental results, indicating the strong influences of defects on compressive stiffness and strength (see Table 2). It is also noted that this model represents the typical behaviour of over-prediction so often observed for FE modelling results.

The failure model of the ideal FE model exhibits a symmetric double shear band deformation due to its perfect geometric symmetry (see Fig. 5(b) ideal FE results), which differs from the experimental observations as the defects break the symmetry and trigger non-symmetrical deformations, i.e., a single shear band, as seen in Fig. 5(b) for the experimental

data. In the densification range for compressive strain higher than 0.7, the curve of ideal lattice simulation converges to the experimental one, indicating that manufacturing defects have minor influences on the densification behaviour of lattices.

4.5 Defect sensitivity of Young's modulus

The defect sensitivity of the Young's modulus of P-shell lattices is investigated via parametric studies utilizing the linear FE model of the full structure. The effects of both individual and combined defects are studied in the order of wall thickness variation, surface roughness, hole defects and waviness.

Firstly, the wall thickness variations as per XCT measurements are considered as the only defect and mapped to the FE model, leading to a Young's modulus normalized by that of the ideal model E/E_0=95.8 %. The results reveal that the thickness variations with standard deviations within 17.6-22.0 µm lead to a reduction of the Young's modulus of about 4.2 % compared to the ideal model.

The influences of surface roughness with various S_a values are investigated next. It is noted that twice of the roughness magnitude is deducted from the shell thicknesses as the shells have two surfaces. The normalized Young's modulus, E/E_0, with respect to surface roughness normalized by the average wall thickness, S_a/t, is shown in Fig. 6 (a). Two imperfect models are studied: models with (1) uniform thicknesses (denoted by UT) and surface roughness (denoted by S_a), and (2) combined variable thicknesses (denoted by VT) and surface roughness. The reduction in property due to each type of defect is visualized by the shaded regions. Fig. 6 (a) shows that both imperfect models exhibit a nearly linear relationship of normalized Young's modulus to normalized surface roughness with a slope of -2.23 for the "UT+S_a" model, and -2.28 for the "VT+S_a" model. The linear relation is attributed to the stretching dominated behaviour of low-density P-shell lattices, which leads to nearly linear scaling of the Young's modulus with respect to the thickness and relative density. As can be seen in Fig. 6 (a), the two lines are almost parallel, indicating that the influences of thickness variations and surface roughness on the Young's modulus can be considered independent to each other. In addition, surface roughness exhibits a stronger impact on the Young's modulus than thickness variations. For example, a uniform roughness of 13.3 µm (S_a/t=0.12) lead to a reduction of E/E_0 of about 28 %, which is much higher than the effect of thickness variations.

In the proposed FE model, the locations and sizes of holes depend on both the thickness distributions and the threshold chosen for element deletion. The regions with small thicknesses

are more likely to be considered as holes with an increase of the threshold values. Based on the wall thickness analysis results, the normalized hole area, A_h/A_0, is calculated for a range of threshold values (see Table 3). After deleting the identified elements, the normalized Young's moduli of the imperfect lattices are computed to study the influences of individual hole defects, thickness variations and surface roughness as well as their combinations. To study the influence of combined geometric defects, the surface roughness is kept constant at two set values of 8.3 and 13.3 μm, corresponding to the measured average roughness and the average powder size, respectively. The simulation results (Fig. 6 (b)) again indicate that the normalized Young's modulus scales nearly linear with normalized hole area for $A_h/A_0 \leq 0.2$ %. The fitted slopes corresponding to the individual hole defects (denoted by "UT+Holes") and "VT+Holes" are close, highlighting that the hole defects have almost no interaction with the thickness variations on the Young's modulus. After the additional surface roughness is included, the fitted slopes slightly decrease from 2.78 to 2.12. Nevertheless, the reductions of Young's modulus due to hole defects and surface roughness change only marginally when both defects are included simultaneously (as shown in the shaded regions in Fig. 6 (b)), indicating that their interactions are minor. The existence of holes with the area of $A_h/A_0 = 0.2$ % leads to a reduction of about 0.42 % - 0.55 % in Young's modulus. Based on the XCT inspection, the hole area is small compared to the total mid-surface area, and thus such a small amount of holes is found to have a minor impact on the Young's modulus of P-shell lattices. With increasing hole areas, the property reduction due to hole defects becomes nonlinear and their effects exhibit interactions with other defects as the fitted slopes for $A_h/A_0 \leq 1.2$ % gradually increase to 3.87 and 2.84 for the models of "UT+Holes" and "VT+Holes+S_a=13.3 μm", respectively.

Table 3. Hole areas of the full FE model with respect to the chosen threshold value.

Threshold, t_{min} (μm)	Hole area, A_h (mm^2)	Normalized hole area, A_h/A_0 (%)
40	0.85	0.02
45	2.36	0.05
50	5.81	0.12
55	12.55	0.27
60	27.13	0.58
65	56.67	1.20

The surface waviness is generated by uniformly distributed random numbers and described by two parameters, i.e., the range and the spatial interval of the random numbers, corresponding to the magnitude and "wavelength" of waviness. In this work, surface waviness with the normalized magnitude M/t ranging 0-2, and normalized spatial interval I/a ranging 0.125-0.5 are investigated. Since the proposed waviness includes randomness, the average and standard deviations from five attempts are plotted for each data point in Fig. 6 (c, d). It is noted that the standard deviations are considered small compared to the property reduction.

Firstly, the individual effect of waviness is studied as shown in Figure 7 (c), without the inclusion of other defects. For a slowly varying waviness, i.e., large spatial intervals, the reduction of the Young's modulus is minor with magnitudes up to twice of the wall thickness. For example, the waviness with a normalized spatial interval I/a=0.5 leads to an average reduction of less than 0.5 % as can be seen in Fig. 6 (c). On the contrary, models with fast varying waviness, i.e., small spatial intervals, exhibit significant reductions in the Young's modulus. For example, the waviness with a normalized spatial interval I/a=0.125 leads to a stiffness reduction of about 15 % at a normalized magnitude of M/t=2. In addition, the reduction of Young's modulus with waviness magnitude is nonlinear, and the slope increases with the magnitude.

Next, the Young's modulus property variations predicted by the imperfect FE models with combined waviness and thickness variations are shown in Fig. 6 (c) for comparison. The curves with uniform and variable thicknesses are parallel with a distance of about 3.9 % - 4.7 %, which is consistent with the individual effect of thickness variation, indicating that the two considered defects act mostly independently. In Fig. 6 (d), the surface roughness values of S_a=13.3 μm (S_a/t=0.12) is combined with waviness and thickness variations. The simulation results show that the Young's modulus is reduced by about 28 % after the surface roughness is incorporated (see the orange shaded region). The comparison of the individual and combined effects of roughness on the Young's modulus of P-shell lattices indicates that effects of surface roughness are independent of waviness. In addition, holes with area of A_h/A_0 = 0.2 % are combined with the other three types of defects, which leads to a minor reduction of the Young's modulus of about 0.2 - 0.4 % (see the light magenta shaded region). All the simulation results on the individual and combined defects reveal that the influences of the four types of defects have minor interactions as long as the hole areas are small, and mostly act in a superposed manner on the Young's modulus of P-shell lattices. Lastly, with all these defects incorporated in FE models, the FE predicted Young's modulus reduces to about 60 % of the ideal value, which is

now much closer to the experimental results. The remaining discrepancy between the FE and experimental Young's modulus may be attributed to the deviations of the generated random waviness and the actual defects in terms of the pattern, magnitude, and "wavelength", and the deviations of the uniform roughness assumption compared with non-uniformly distributed roughness in printed samples. Another contributing reason for the discrepancy is that the experimental Young's modulus was obtained from the loading slope of compressive tests, which may underestimate the Young's modulus of lattices due to the influence of non-flat contact surfaces and onset of local yielding. The measurement of the Young's modulus of lattices from the unloading slope of compressive tests has been shown to achieve more accurate results in comparison to FE analysis [38].

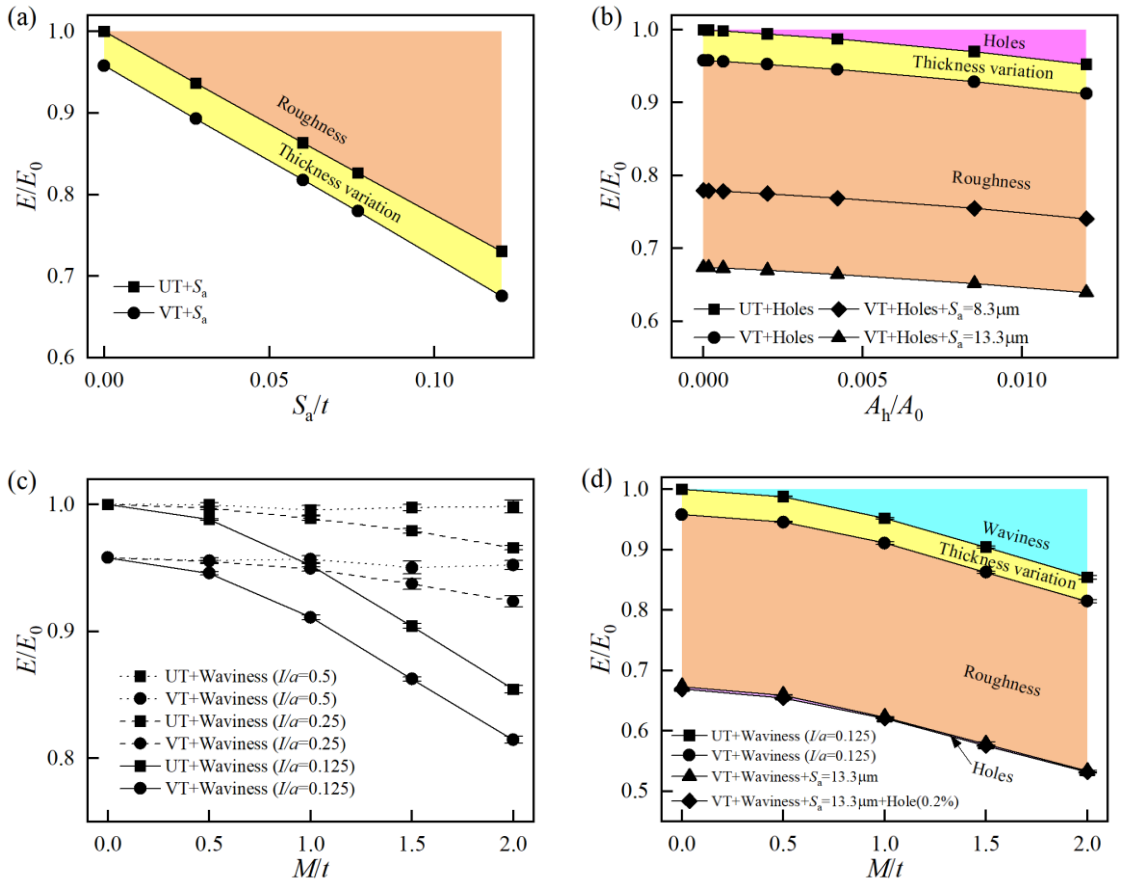

Fig. 6. Defect sensitivities of the Young's modulus of P-shell lattices based on parametric defect studies. (a) Normalized Young's modulus vs. normalized surface roughness. (b) Normalized Young's modulus vs. normalized hole area. (c, d) Normalized Young's modulus vs. normalized waviness magnitude. The influence of each type of geometric defect is shaded by different colours.

4.6 Defect sensitivity of nonlinear and failure behaviour

Nonlinear compression simulations are conducted to study the sensitivity of the failure characteristics and densification behaviour along the *z*-direction to the defect types and magnitudes. Due to the high computational costs of nonlinear simulations (200-500 hours CPU time per job), several representative magnitudes and combinations of defects are selected and their influence on the first peak stress, plateau stress which is defined as the average stress within 0.2-0.4 compressive strains [42], energy absorption capacity, stress-strain response, and failure deformation are compared.

In the first series of simulations, the ideal model and the imperfect model with only thickness variations are analysed. Compared to the ideal model, the first peak stress of the model with thickness variations reduces from 12.20 MPa to 11.25 MPa (7.8 % reduction) and the plateau stress reduces from 9.26 MPa to 8.52 MPa (8.0% reduction) as shown in Fig. 5 and Table 2. In the densification region of the stress-strain curves, the curves of the imperfect models are almost the same as those of the ideal model and experiments at a compressive strain above 0.7. This is because the densification behaviour is determined by the contact of shells and all the models/structures have the same average shell thickness and relative density. Most notably, the shell thickness variations break the mirror symmetry of lattice samples, leading to asymmetric nonlinear deformations. As a result, the imperfect model with thickness variations displays an asymmetric, single shear band deformation under large compressive strains (Figs. 8 (a, b)), which is also observed during the experimental tests.

In the second series of simulations, surface waviness with a series of magnitudes and "frequencies" are superimposed onto the earlier XCT-based thickness variations. With a fixed wave magnitude M/t=1 and varying the spatial interval I/a from 0.125 to 0.5, the change of peak stresses is less than 1.5%, indicating that the peak stress is nearly independent of wave interval (Fig. 7 (a)). With the decrease of spatial interval, the stress fluctuations become milder in the plateau region. The interval has minor influence on the plateau stress, i.e., the arithmetic average of stress fluctuations, as the changes due to I/a varying from 0.125 to 0.5 are less than 4.5%. Fig. 7 (c) illustrates the effect of a fixed interval I/a=0.125 and varying wave magnitude M/t from 0 to 2. It is found that the stress-strain curve and mechanical properties of the model with M/t=0.5 are nearly identical to the one without waviness; with an increase of the wave magnitude up to M/t=2, the influences on both the first peak stress and plateau stress are marginal, and the stress fluctuations in the plateau region become milder. From the deformations of imperfect lattices (Fig. 7 (b, d)), it is seen that waviness with magnitudes equal

or larger than the average shell thickness results in prominent single shear band deformations, which agrees better with experimental deformations. For the densification region of the stress-strain curves, nonlinear simulation results indicate that the waviness has negligible effects on the densification behaviour of shell lattices because the shell thicknesses remain unchanged.

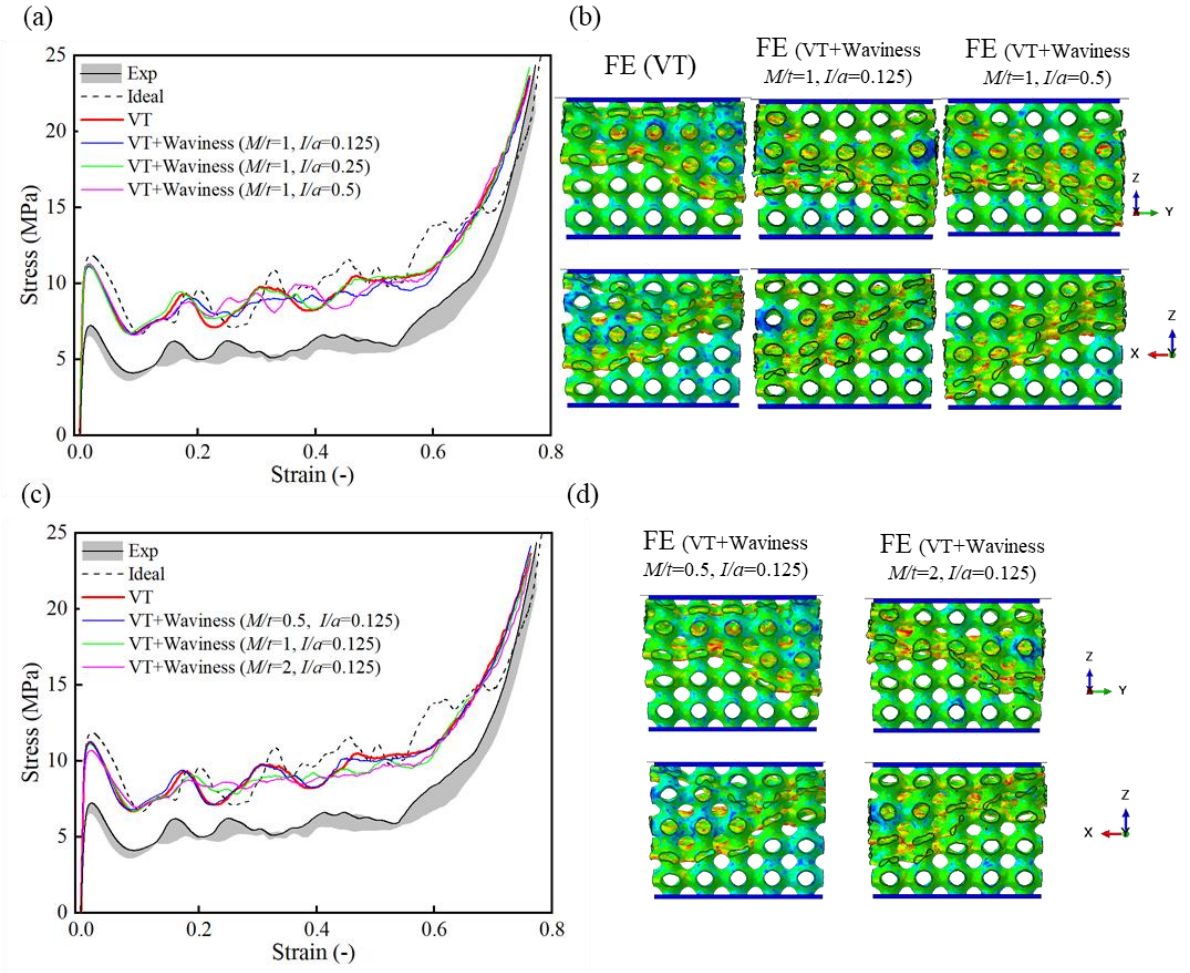

Fig. 7. Influences of thickness variations (VT) and waviness on the nonlinear behaviour of P-shell lattices. (a) Stress-strain curves and (b) deformations at ε=0.24 of P-shell lattices including thickness variations and waviness with different intervals and fixed M/t=1. (c) Stress-strain curves and (d) deformations at ε=0.24 of P-shell lattices including thickness variations and waviness with different magnitudes and fixed I/a=0.125. FE deformations are shaded by contours of von Mises stress σ_v of shells with the same legend in Fig. 5.

In the third series of simulations, the hole defects with different hole areas are superimposed onto thickness variations, in which surface waviness is not included. When compared with the model with only thickness variations, it is found that including a hole area less than 0.27%

leads to almost identical stress-strain responses as shown in Fig. 8. Meanwhile, the influences of first peak stress and plateau stress due to small hole areas are less than 1.5%. When increasing hole areas to 1.2 %, the first peak stress shows a reduction about 6.0% and the failure locations together with the stress-strain behaviour are also slightly changed as can be seen in Fig. 8. The magnified stress plots in Fig. 8 (b) show that some hole defects lead to stress concentrations, while other holes do not.

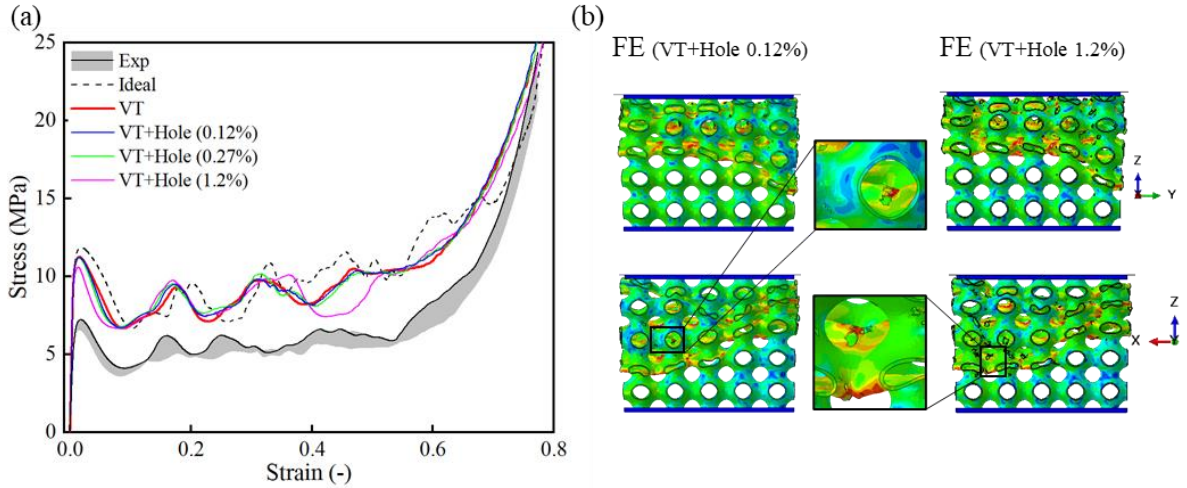

Fig. 8. Influences of hole defects on the nonlinear behaviour of P-shell lattices. (a) Stress-strain curves and (b) deformations at ε=0.24 of P-shell lattices including thickness variations and waviness with different intervals. The magnified plots show the deformations and stresses around holes. FE deformations are shaded by contours of von Mises stress σ_v of shells with the same legend in Fig. 5.

In the fourth series of nonlinear simulations, the surface roughness is superimposed onto thickness variations without surface waviness and holes. Including a total thickness reduction of 16.6 µm (corresponding to the measured average roughness S_a=8.3 µm) onto thickness variation significantly reduces the compressive stresses as can be seen in Fig. 9. The first peak stress and plateau stress are 8.74 MPa and 6.55 MPa, which are both about 71 % of the ideal model. For a total thickness reduction of 26.6 µm (corresponding to S_a=13.3 µm, the average powder size), the first peak stress and plateau stress reduce to 59 % and 60 % of the ideal model, respectively. The comparison with testing results indicates that the thickness reduction of 26.6 µm leads to the stress-strain responses of the numerical FE models falling into the experimental variation domain. Since the shell structural thickness reduction is considered uniform, the failure deformations are similar to the FE models with only thickness variations (Fig. 9 (b)). The influences of surface elements are shown by the two stress-strain curves with and without

surface elements in Fig. 9 (a). It is found that the stress-strain behaviour is almost identical for the two models until the onset of densification. The absence of surface elements delays the shell contact and leads to minor discrepancies between the two curves within the stress plateau region. The effect of including the surface elements representing the roughness contact becomes more prominent with increasing contact regions. In the densification region, which is dominated by shell contact, the stresses without surface elements are consistently lower due to the delayed contact. The incorporation of surface elements, which represent the contact behaviour of a rough surface but do not contribute to the mechanical stiffness and strength, can therefore correct the contact behaviour in the defect-informed FE models, and this plays an important role when predicting the stress increase in the large compression deformation and densification regions.

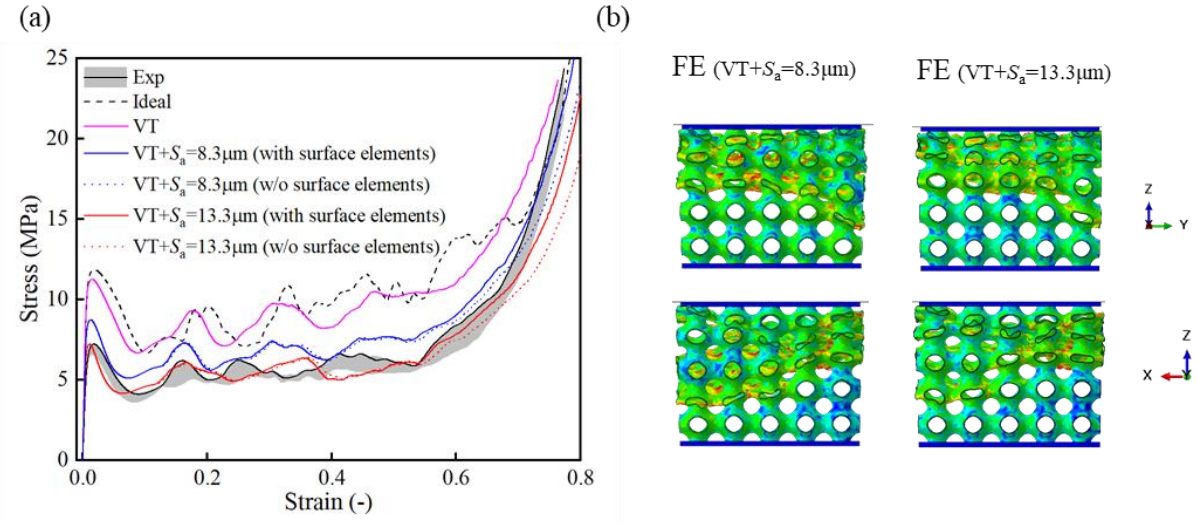

Fig. 9. Influences of surface roughness on the nonlinear behaviour of P-shell lattices. (a) Stress-strain curves and (b) deformations at ε=0.24 of P-shell lattices including thickness variations and surface roughness. FE deformations are shaded by contours of von Mises stress σ_v of shells with the same legend in Fig. 5.

Lastly, thickness variations, surface waviness, roughness, and hole defects are sequentially incorporated into the FE model. Herein, surface roughness of S_a=13.3 μm is adopted due to the good agreement with experimental results. Since the exact values of waviness and holes defects are unknown, moderate magnitudes are adopted based on XCT observations, i.e., M/t = 1, I/a = 0.125, and A_h/A_0 = 0.12 %. The stress-strain responses and deformations are shown in Fig. 10 and the compressive properties are listed in Table 1. Compared with the ideal model,

thickness variations lead to reduced peak and plateau stresses. When including surface waviness, the stress plateau is flattened, while the peak and plateau stresses remain unchanged. The further introduced surface roughness leads to major reductions of peak and plateau stresses. The finally introduced hole defects exhibits minor influences on the compressive properties. With all the geometric defects incorporated, the stress-strain curve of the imperfect shell lattice falls into the experimental variation domain; the prediction error of peak and plateau stresses are less than 5%; and the deformations feature non-symmetric single shear bands which are close to experiments. It is also noted that this imperfect model is able to capture the single shear band collapse behaviour as can be seen in the FE deformation at the compressive strain of 0.15 (Fig. 10 (b)), and thereafter the discrepancies for peak and deformation predictions increase, but this is expected for the complex nonlinear models.

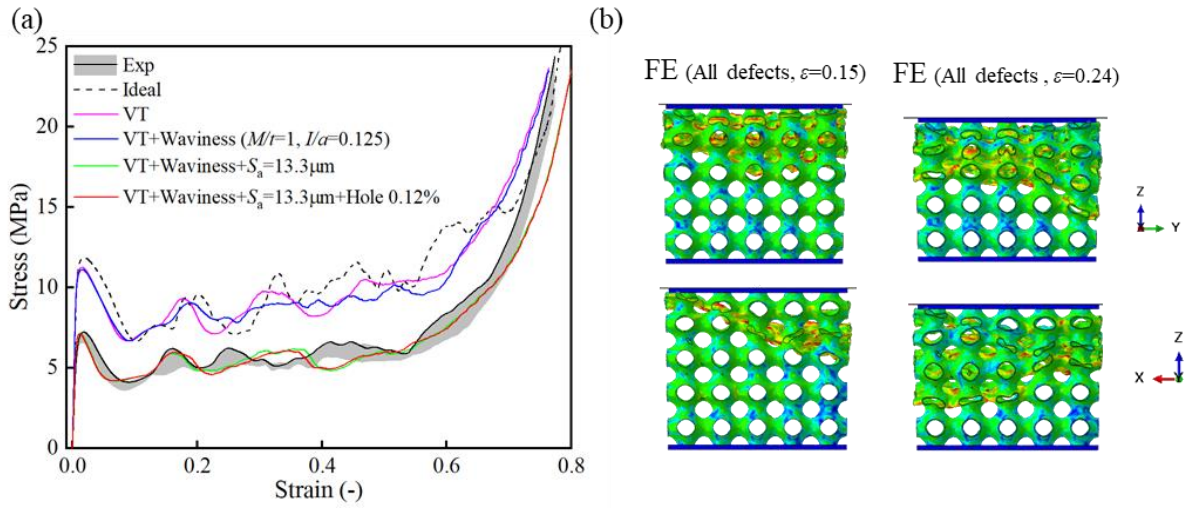

Fig. 10. Influences of all geometric defects on the nonlinear behaviour of P-shell lattices. (a) Stress-strain curves and (b) deformations at ε=0.15 and 0.24 of P-shell lattices. FE deformations are shaded by contours of von Mises stress σ_v of shells with the same legend in Fig. 5.

4.7 Discussion

The simulation results reveal that each type of geometric defects has different influences on the linear and nonlinear properties of P-shell lattices. For the Young's modulus, the four types of defects do not interact to each other, and their effects can be superimposed as clearly highlighted in the parametric defect studies. Based on the quantitative analysis, the reduction due to thickness variations with standard deviations around 17-22 μm is about 4 %. The

sensitivity of Youngs modulus (represented by the slopes in Fig. 6 (a, b)) with respect to holes is larger than for the surface roughness, but the magnitude of holes A_h/A_0 is generally one order of magnitude smaller than that of the surface roughness S_a/t. As a result, the surface roughness exhibits a significant reduction of Young's modulus (up to 28 % at $S_a/t = 0.12$) compared with holes (about 5 % at $A_h/A_0 = 1.2$ %).

Since shell lattices have very large surface area, a small variation in thickness leads to significant changes of the mechanical properties, especially for thin-walled structures. For waviness with low spatial "frequency", i.e., large spatial intervals, the reductions of the Young's modulus are minor; but in contrast, rapidly varying waviness, i.e., small spatial intervals, can dramatically reduce the Young's modulus of lattices. For μLPBF fabricated thin-wall shell lattices, the waviness and the magnitude of waviness may be comparable to the unit cell size and wall thickness for thin-walled structures, respectively (see Fig. 1), due to overhang and thermal distortions; hence the potential influence of waviness on the Young's modulus is considered significant.

For the nonlinear and failure behaviour, the thickness variation and surface roughness play important roles for the first stress peak and plateau stress, while holes and waviness do not. The reductions of the first stress peak and plateau stress due to the thickness variation are both about 8 %. The stress reductions due to surface roughness of 8.3 and 13.3 um are about 30 % and 40 %, respectively. The densification behaviour is mostly determined by the shell/strut thickness for a given lattice topology according to the theory of cellular solids [43]. Since none of the geometric defects studied in this work affect the average shell thickness of lattices to a great extent in which the thickness reduction is compensated by surface elements, the densification behaviour predicted by the proposed FE model agrees well with experimental results. With the improved prediction accuracy for plateau stress and densification behaviour, the energy absorption capacity can now also be well predicted.

The failure deformations observed from experiments exhibit a single shear band, which is non-symmetric. The defects of thickness variations, holes, and waviness tend to break the symmetry and result in non-symmetric deformations, which are consistent with experiments. We note that the thickness variation is more likely to lead to non-symmetric deformations for thin-walled shell lattices than thick-walled ones. For higher shell thicknesses and relative densities such as 18.2 %, the P-shell lattices experimentally displayed symmetric double shear band mode even if thickness variations existed [4].

The above findings result in important outcomes for quality control and assurance. According to the abovementioned defect sensitivity analysis, it is interesting to find that small amounts of holes have only minor influences (less than 1%) on linear and nonlinear properties of P-shell lattices. It follows that structures used to bear static loading do not need to be discarded during a post-process quality control check if minor hole defects are found, unless a physically intact wall structure is required for applications with flow phase separation. The same finding applies for slowly varying surface waviness with small magnitudes. Thickness variations have significant influences on the compressive properties. Surface roughness plays an important role for all the compressive properties, i.e., Young's modulus, peak and plateau strength, of P-shell lattices. Therefore, efforts from fabrication processes including process optimization and post-processing such as sand blasting and polishing should be given a high priority for structural applications to improve the mechanical performance and for weight reduction [44–46]. As roughness is an inherent process feature that is difficult to remove during LPBF processes, investigations of surface roughness distributions of complex 3D structures as well as the dependency on geometric features are required to further contribute to the understanding towards the causes and effects of surface roughness. For example, Jones et al. conducted a comprehensive study on the effect of surface curvature and inclination angle on surface quality and roughness for LPBF fabricated curved thin shell structures [21]. The detailed characterization of surface roughness for shell lattices will facilitate the accurate prediction of their mechanical properties. Finally, it is noted the waviness was not quantitatively measured in this work as the determination of the mid-surface of shell lattices from CT data remains a challenge.

5. Conclusions

Finite element analysis of complex structures generally results in overestimation for structural performance prediction due to the assumption of an ideal printed geometry. To overcome this drawback of numerical modelling, this paper presents validated quantitative analysis of the influences of geometric defects (thickness variations, holes, waviness, and surface roughness) on the compressive properties (Young's modulus, peak stress, plateau stress, and failure behaviour) of μLPBF fabricated thin shell lattices. P-shell lattices with an average thickness of 108.0 μm were fabricated by μLPBF from SS316L powders. The thickness variations and surface roughness of as-printed lattices were characterized by XCT scanning

and subsequent detailed data analysis to enable accurate mapping of defects within the numerical model.

To study the defect sensitivities of compressive properties, we proposed an XCT-based, variable shell thickness FE modelling method for thin shell lattices to capture the four main types of geometric defects for high-fidelity simulations. In addition, the proposed FE model enabled parametric studies via activation and deactivation of each type of defect as well as the manipulation of their magnitudes and frequencies. The combined evaluation of simulation and compression testing results indicates that the proposed FE models exhibits a significantly improved agreement with testing results. The main findings from defect characterization and sensitivity analysis are:

1. Our detailed analysis of the μLPBF processes highlighted the successful fabrication of thin shell lattices with average shell thickness down to 108 μm with standard deviations around 17-22 μm, and upward and downward surface roughness around a value of S_a of 5.5 μm and 11.1 μm, respectively.
2. The thickness variations with standard deviations around 17-22 μm lead to reductions of Young's modulus, peak stress, and plateau stress around 4 %, 8 %, and 8 %, respectively.
3. Surface roughness can reduce the Young's modules, peak and plateau stresses by more than 20 % as the attached particles do not contribute to the mechanical properties as a solid material layer, indicating that reducing the surface roughness may be a promising and efficient way to improve the mechanical properties of LPBF fabricated thin shell lattices.
4. A small amount of holes (< 0.2 % of the total surface area) has minor influences on the compressive properties of P-shell lattices, indicating that this defect is not critical for static properties.
5. Rapidly varying surface waviness can significantly reduce the Young's modulus of P-shell lattices, while the investigated surface waviness range with various magnitudes and spatial frequencies had a minor influence on the peak and plateau stresses.

The findings presented here are valid for P-shell type structures. Other TPMS types, such as Gyroid, Diamond, and others, might respond differently to geometric defects. Nevertheless, the proposed methodology of XCT-based FE analysis coupled with defect sensitivity studies is highly flexible to adapt to other types of shell element structures. The more detailed

characterization and modelling of both geometrically and material imperfect 3D structures will be considered in our future works.

Acknowledgments

The authors acknowledge the support from the Agency for Science, Technology and Research (A*STAR) and the Science and Engineering Research Council (SERC) of Singapore through the Additive Manufacturing Centre (AMC) Initiative – SIMTech-led R&D projects (SERC Grant no. 142 68 00088). The authors are grateful to SIMTech staff Mr. Ong Wee Kit for his assistance on XCT scanning.

Appendix A Mesh refinement study of the ideal P-shell lattice

A mesh refinement study is conducted to investigate the influence of mesh density on the mechanical properties of the structure of interest and to identify an optimal mesh density that balances the accuracy of FE results and computational costs. Here, we use the ideal P-shell lattices with a thickness of 108.0 μm for the mesh refinement study. The geometry model includes a uniform P-shell lattice core (S3/S3R) and two face plates (C3D8R). Linear simulation models are used to calculate the Young's modulus, and nonlinear models are used to evaluate nonlinear properties and failure behaviour. A wide range of mesh densities of the P-shell lattice core is investigated, ranging from 37K nodes and 72K elements to 1.038M nodes and 2.062M elements. The mesh, mechanical properties, and stress-strain responses are shown in Fig. A1, and Table A1. Using the finest mesh as benchmark, the selected mesh (190K nodes and 370K elements) in this work shows minor differences in terms of Young's modulus (+1.57%), peak stress (+2.47%), plateau stress (+4.26%), as well as the overall stress-strain curve characteristics. Therefore, this mesh is adopted in the current defect sensitivity analysis to achieve a balance between computational efficiency and analysis accuracy.

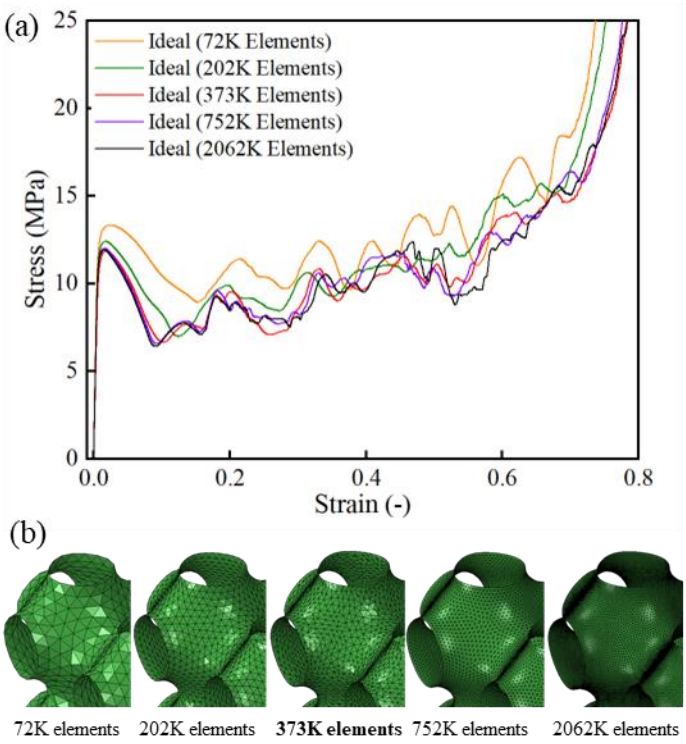

Fig. A1 Results of mesh refinement study: (a) stress-strain curves and (b) mesh of uniform P-shell lattices with different mesh densities.

Table A1 Compressive properties of ideal P-shell lattice with different mesh densities. The model with 1.038M nodes and 2.062M elements is adopted as benchmark. Percentage differences with respect to the benchmark are shown in brackets.

Number of nodes	Number of elements	Area of mesh (mm^2)	Young's modulus (GPa)	Peak stress (MPa)	Plateau stress (MPa)
1.038M	2.062M	4708 (0.00%)	1.959 (0.00%)	11.91 (0.00%)	8.88 (0.00%)
380K	752K	4710 (+0.05%)	1.968 (+0.48%)	12.01 (+0.88%)	9.16 (+3.06%)
190K	**373K**	**4714 (+0.13%)**	**1.990 (+1.57%)**	**12.20 (+2.47%)**	**9.26 (+4.26%)**
103K	202K	4720 (+0.26%)	2.005 (+2.36%)	12.41 (+4.19%)	9.62 (+8.24%)
37K	72K	4745 (+0.80%)	2.092 (+6.79%)	13.34 (+12.00%)	10.92 (+22.96%)

References

[1] O. Al-Ketan, R.K. Abu Al-Rub, Multifunctional Mechanical Metamaterials Based on Triply Periodic Minimal Surface Lattices, Adv. Eng. Mater. 21 (2019) 1–39. https://doi.org/10.1002/adem.201900524.

[2] C. Bonatti, D. Mohr, Mechanical performance of additively-manufactured anisotropic and isotropic smooth shell-lattice materials: Simulations & experiments, J. Mech. Phys. Solids. 122 (2019) 1–26. https://doi.org/10.1016/j.jmps.2018.08.022.

[3] O. Al-Ketan, R. Rowshan, R.K. Abu Al-Rub, Topology-mechanical property relationship of 3D printed strut, skeletal, and sheet based periodic metallic cellular materials, Addit. Manuf. 19 (2018) 167–183. https://doi.org/10.1016/j.addma.2017.12.006.

[4] L. Zhang, S. Feih, S. Daynes, S. Chang, M.Y. Wang, J. Wei, W.F. Lu, Energy absorption characteristics of metallic triply periodic minimal surface sheet structures under compressive loading, Addit. Manuf. 23 (2018) 505–515. https://doi.org/10.1016/j.addma.2018.08.007.

[5] S.C. Han, J.W. Lee, K. Kang, A New Type of Low Density Material: Shellular, Adv. Mater. 27 (2015) 5506–5511. https://doi.org/10.1002/adma.201501546.

[6] S. Mohammad, J. Razavi, M. Benedetti, S. Murchio, M. Leary, M. Watson, D. Bhate, F. Berto, Progress in Materials Science Properties and applications of additively manufactured metallic cellular materials : A review, Prog. Mater. Sci. 125 (2022) 100918. https://doi.org/10.1016/j.pmatsci.2021.100918.

[7] M.G. Rashed, M. Ashraf, R.A.W. Mines, P.J. Hazell, Metallic microlattice materials: A current state of the art on manufacturing, mechanical properties and applications, Mater. Des. 95 (2016) 518–533. https://doi.org/10.1016/j.matdes.2016.01.146.

[8] B. Blakey-milner, P. Gradl, G. Snedden, M. Brooks, J. Pitot, E. Lopez, M. Leary, F. Berto, Metal additive manufacturing in aerospace : A review, Mater. Des. 209 (2021) 110008. https://doi.org/10.1016/j.matdes.2021.110008.

[9] B. Nagarajan, Z. Hu, X. Song, W. Zhai, J. Wei, Development of Micro Selective Laser Melting : The State of the Art and Future Perspectives, Engineering. 5 (2019) 702–720. https://doi.org/10.1016/j.eng.2019.07.002.

[10] D. Gu, X. Shi, R. Poprawe, D.L. Bourell, R. Setchi, J. Zhu, R. Summary, Material-structure-performance integrated laser-metal additive manufacturing, Science. 372 (2021). https://doi.org/10.1126/science.abg1487.

[11] L.Y. Chen, S.X. Liang, Y. Liu, L.C. Zhang, Additive manufacturing of metallic lattice structures: Unconstrained design, accurate fabrication, fascinated performances, and challenges, Mater. Sci. Eng. R Reports. 146 (2021) 100648. https://doi.org/10.1016/j.mser.2021.100648.

[12] Y. Kok, X.P. Tan, P. Wang, M.L.S. Nai, N.H. Loh, E. Liu, S.B. Tor, Anisotropy and heterogeneity of microstructure and mechanical properties in metal additive manufacturing : A critical review, Mater. Des. 139 (2018) 565–586. https://doi.org/10.1016/j.matdes.2017.11.021.

[13] N. Sanaei, A. Fatemi, Progress in Materials Science Defects in additive manufactured metals and their effect on fatigue performance : A state-of-the-art review, Prog. Mater. Sci. 117 (2021) 100724. https://doi.org/10.1016/j.pmatsci.2020.100724.

[14] A. du Plessis, I. Yadroitsava, I. Yadroitsev, Effects of defects on mechanical properties in metal additive manufacturing: A review focusing on X-ray tomography insights, Mater. Des. 187 (2020) 108385. https://doi.org/10.1016/j.matdes.2019.108385.

[15] J. Fu, H. Li, X. Song, M.W. Fu, Multi-scale defects in powder-based additively manufactured metals and alloys, J. Mater. Sci. Technol. 122 (2022) 165–199. https://doi.org/10.1016/j.jmst.2022.02.015.

[16] Y. Amani, S. Dancette, P. Delroisse, A. Simar, E. Maire, Compression behavior of lattice structures produced by selective laser melting: X-ray tomography based experimental and finite element approaches, Acta Mater. 159 (2018) 395–407. https://doi.org/10.1016/j.actamat.2018.08.030.

[17] D. Pasini, J.K. Guest, Imperfect architected materials: Mechanics and topology optimization, MRS Bull. 44 (2019) 766–772. https://doi.org/10.1557/mrs.2019.231.

[18] H. Lei, C. Li, J. Meng, H. Zhou, Y. Liu, X. Zhang, P. Wang, D. Fang, Evaluation of compressive properties of SLM-fabricated multi-layer lattice structures by experimental test and μ-CT-based finite element analysis, Mater. Des. 169 (2019). https://doi.org/10.1016/j.matdes.2019.107685.

[19] L. Liu, P. Kamm, F. García-Moreno, J. Banhart, D. Pasini, Elastic and failure response of imperfect three-dimensional metallic lattices: the role of geometric defects induced by Selective Laser Melting, J. Mech. Phys. Solids. 107 (2017) 160–184. https://doi.org/10.1016/j.jmps.2017.07.003.

[20] G. Campoli, M.S. Borleffs, S. Amin Yavari, R. Wauthle, H. Weinans, A.A. Zadpoor, Mechanical properties of open-cell metallic biomaterials manufactured using additive

manufacturing, Mater. Des. 49 (2013) 957–965. https://doi.org/10.1016/j.matdes.2013.01.071.

[21] A. Jones, M. Leary, S. Bateman, M. Easton, Effect of surface geometry on laser powder bed fusion defects, J. Mater. Process. Tech. 296 (2021) 117179. https://doi.org/10.1016/j.jmatprotec.2021.117179.

[22] A. Alghamdi, D. Downing, R. Tino, A. Almalki, T. Maconachie, B. Lozanovski, M. Brandt, M. Qian, M. Leary, Buckling phenomena in AM lattice strut elements: A design tool applied to Ti-6Al-4V LB-PBF, Mater. Des. 208 (2021) 109892. https://doi.org/10.1016/j.matdes.2021.109892.

[23] F. Zanini, M. Sorgato, E. Savio, S. Carmignato, Dimensional verification of metal additively manufactured lattice structures by X-ray computed tomography: Use of a newly developed calibrated artefact to achieve metrological traceability, Addit. Manuf. 47 (2021) 102229. https://doi.org/10.1016/j.addma.2021.102229.

[24] J.S. Rathore, C. Mang, C. Vienne, Y. Quinsat, C. Tournier, A methodology for computed tomography-based nondestructive geometrical evaluations of lattice structures by holistic strut measurement approach, J. Manuf. Sci. Eng. Trans. ASME. 143 (2021) 1–12. https://doi.org/10.1115/1.4049492.

[25] J.L. Grenestedt, Influence of wavy imperfections in cell walls on elastic stiffness of cellular solids, J. Mech. Phys. Solids. 46 (1998) 29–50. https://doi.org/10.1016/S1359-6462(98)00401-1.

[26] M. Dallago, B. Winiarski, F. Zanini, S. Carmignato, M. Benedetti, On the effect of geometrical imperfections and defects on the fatigue strength of cellular lattice structures additively manufactured via Selective Laser Melting, Int. J. Fatigue. 124 (2019) 348–360. https://doi.org/10.1016/j.ijfatigue.2019.03.019.

[27] L. Xiao, S. Li, W. Song, X. Xu, S. Gao, Process-induced geometric defect sensitivity of Ti–6Al–4V lattice structures with different mesoscopic topologies fabricated by electron beam melting, Mater. Sci. Eng. A. 778 (2020) 139092. https://doi.org/10.1016/j.msea.2020.139092.

[28] N. Korshunova, G. Alaimo, S.B. Hosseini, M. Carraturo, A. Reali, J. Niiranen, F. Auricchio, E. Rank, S. Kollmannsberger, Bending behavior of octet-truss lattice structures: Modelling options, numerical characterization and experimental validation, Mater. Des. 205 (2021) 109693. https://doi.org/10.1016/j.matdes.2021.109693.

[29] N. Korshunova, G. Alaimo, S.B. Hosseini, M. Carraturo, A. Reali, J. Niiranen, F.

Auricchio, E. Rank, S. Kollmannsberger, Image-based numerical characterization and experimental validation of tensile behavior of octet-truss lattice structures, Addit. Manuf. 41 (2021) 101949. https://doi.org/10.1016/j.addma.2021.101949.

[30] A. du Plessis, G. Schwaderer, I. Cristofolini, M. Zago, M. Benedetti, Dimensional metrology of additively manufactured lattice structures by combined tactile probe and X-ray tomography, Mater. Des. Process. Commun. 3 (2021) 1–12. https://doi.org/10.1002/mdp2.216.

[31] S. Youssef, E. Maire, R. Gaertner, Finite element modelling of the actual structure of cellular materials determined by X-ray tomography, Acta Mater. 53 (2005) 719–730. https://doi.org/10.1016/j.actamat.2004.10.024.

[32] E. Liverani, F. Zanini, L. Tonelli, S. Carmignato, A. Fortunato, The influence of geometric defects and microstructure in the simulation of the mechanical behaviour of laser powder-bed fusion components: Application to endoprosthesis, J. Manuf. Process. 71 (2021) 541–549. https://doi.org/10.1016/j.jmapro.2021.09.043.

[33] D. Melancon, Z.S. Bagheri, R.B. Johnston, L. Liu, M. Tanzer, D. Pasini, Mechanical characterization of structurally porous biomaterials built via additive manufacturing: experiments, predictive models, and design maps for load-bearing bone replacement implants, Acta Biomater. 63 (2017) 350–368. https://doi.org/10.1016/j.actbio.2017.09.013.

[34] X. Cao, Z. Huang, C. He, W. Wu, L. Xi, Y. Li, D. Fang, In-situ synchrotron X-ray tomography investigation of the imperfect smooth-shell cylinder structure, Compos. Struct. 267 (2021). https://doi.org/10.1016/j.compstruct.2021.113926.

[35] N. Korshunova, I. Papaioannou, S. Kollmannsberger, D. Straub, E. Rank, Uncertainty quantification of microstructure variability and mechanical behavior of additively manufactured lattice structures, Comput. Methods Appl. Mech. Eng. 385 (2021) 114049. https://doi.org/10.1016/j.cma.2021.114049.

[36] B.C. White, A. Garland, B.L. Boyce, Topological homogenization of metamaterial variability, Mater. Today. In press (2022). https://doi.org/10.1016/j.mattod.2022.01.021.

[37] B. Lozanovski, D. Downing, P. Tran, D. Shidid, M. Qian, P. Choong, M. Brandt, M. Leary, A Monte Carlo simulation-based approach to realistic modelling of additively manufactured lattice structures, Addit. Manuf. 32 (2020) 101092. https://doi.org/10.1016/j.addma.2020.101092.

[38] L. Zhang, Z. Hu, M.Y. Wang, S. Feih, M. Yu Wang, S. Feih, Hierarchical sheet triply

periodic minimal surface lattices: design, geometric and mechanical performance, Mater. Des. 209 (2021) 109931. https://doi.org/10.1016/j.matdes.2021.109931.

[39] I. Amidror, Scattered data interpolation methods for electronic imaging systems: a survey, J. Electron. Imaging. 11 (2002) 157. https://doi.org/10.1117/1.1455013.

[40] R. Hong, L. Zhang, J. Lifton, S. Daynes, J. Wei, S. Feih, W.F. Feng, W.F. Lu, Artificial neural network-based geometry compensation to improve the printing accuracy of selective laser melting fabricated sub-millimetre overhang trusses, Addit. Manuf. 37 (2021) 101594. https://doi.org/10.1016/j.addma.2020.101594.

[41] J.J. Lifton, Y. Liu, Z.J. Tan, B. Mutiargo, X.Q. Goh, Internal surface roughness measurement of metal additively manufactured samples via x-ray CT: the influence of surrounding material thickness, Surf. Topogr. Metrol. Prop. 9 (2021) 035008. https://doi.org/10.1088/2051-672X/ac0e7c.

[42] ISO13314:2011, Mechanical Testing of Metals—ductility Testing—compression Test for Porous and Cellular Metals, Int. Organ. Stand. (2011).

[43] L.J. Gibson, M.F. Ashby, Cellular solids: Structure and properties, Cambridge University Press, 2014. https://doi.org/10.1017/CBO9781139878326.

[44] S. Chang, A. Liu, C.Y.A. Ong, L. Zhang, X. Huang, Y.H. Tan, L. Zhao, L. Li, J. Ding, Highly effective smoothening of 3D-printed metal structures via overpotential electrochemical polishing, Mater. Res. Lett. 7 (2019) 282–289. https://doi.org/10.1080/21663831.2019.1601645.

[45] J. Zhang, Y.J. Lee, H. Wang, A Brief Review on the Enhancement of Surface Finish for Metal Additive Manufacturing, J. Miner. Met. Mater. Eng. 7 (2021) 1–14. https://doi.org/https://doi.org/10.31437/2414-2115.2021.07.1.

[46] L. Yang, C. Yan, W. Cao, Z. Liu, B. Song, S. Wen, C. Zhang, Y. Shi, S. Yang, Compression–compression fatigue behaviour of gyroid-type triply periodic minimal surface porous structures fabricated by selective laser melting, Acta Mater. 181 (2019) 49–66. https://doi.org/10.1016/j.actamat.2019.09.042.